ELSEVIER

Earth and Planetary Science Letters 204 (2002) 17–32

EPSL

www.elsevier.com/locate/epsl

Fate of the Cenozoic Farallon slab from a comparison of kinematic thermal modeling with tomographic images

Christian Schmid *, Saskia Goes, Suzan van der Lee, Domenico Giardini

Institute of Geophysics, ETH Hönggerberg (HPP), 8093 Zürich, Switzerland

Received 28 May 2002; received in revised form 11 September 2002; accepted 18 September 2002

Abstract

After more than 100 million years of subduction, only small parts of the Farallon plate are still subducting below western North America today. Due to the relatively young age of the most recently subducted parts of the Farallon plate and their high rates of subduction, the subducted lithosphere might be expected to have mostly thermally equilibrated with the surrounding North American mantle. However, images from seismic tomography show positive seismic velocity anomalies, which have been attributed to this subduction, in both the upper and lower mantle beneath North America. We use a three-dimensional kinematic thermal model based on the Cenozoic plate tectonic history to quantify the thermal structure of the subducted Farallon plate in the upper mantle and determine which part of the plate is imaged by seismic tomography. We find that the subducted Farallon lithosphere is not yet thermally equilibrated and that its thermal signature for each time of subduction is found to be presently detectable as positive seismic velocity anomalies by tomography. However, the spatially integrated positive seismic velocity anomalies in tomography exceed the values obtained from the thermal model for a rigid, continuous slab by a factor of 1.5 to 2.0. We conclude that Farallon fragments that subducted since 50 to 60 Ma are still residing in the upper mantle and must be heavily deformed. The deformation of the slab in the transition zone is probably caused by the same mechanisms that were responsible for flat subduction around 60 Ma.

Keywords: Farallon plate; thermo-kinematic modeling; subduction; tomography; upper mantle

1. Introduction

Off the west coast of North America the Farallon plate subducted during most of the Meso- and Cenozoic. The evolution of oceanic tectonic plates at the surface is well known from the analysis of magnetic patterns on the ocean floor, in combination with geological observations on overriding plates. However, the evolution of these plates after their subduction is much less well known and is only inferred indirectly from tomographic images of the present seismic structure of Earth's mantle and from numerical and laboratory experiments. A qualitative comparison of tomographic images with the plate tectonic history of the Farallon plate subducting beneath the North American plate has enabled rough esti-

* Corresponding author. Tel.: +41-1-633-2907; Fax: +41-1-633-1065.
E-mail address: cschmid@tomo.ig.erdw.ethz.ch (C. Schmid).

0012-821X/02/$ – see front matter
PII: S0012-821X(02)00985-8

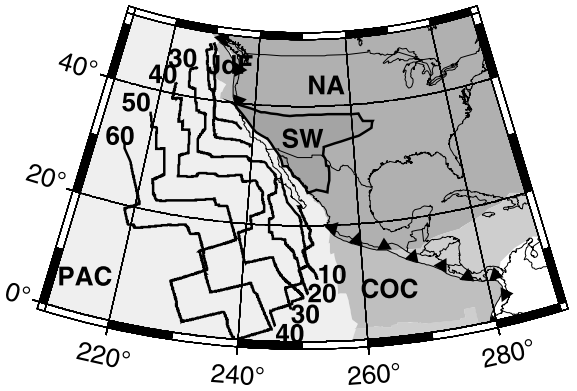

Fig. 1. Map of the study area. Abbreviations: NA, North American plate; PAC, Pacific plate; COC, Cocos plate; JdF, Juan de Fuca plate; SW, the approximate present extent of the slab window, assuming a 0° slab dip. Triangles mark presently active subduction zones. Lines show past positions of the Farallon–Pacific ridge relative to a fixed North America from 60 to 10 Ma, derived from the digital age map of Müller et al. [17] and the poles of Norton [16].

mates of which part of the subducted plate is at which position in the mantle today [1,2]. A more quantitative comparison, involving numerical modeling, has been made for the Mesozoic subduction [3]. Here we extend a study by Van der Lee et al. [4], involving plate tectonic history, seismic tomography, and numerical modeling, to identify the present position in Earth's mantle of the Farallon lithosphere that subducted during the Cenozoic.

During this time the mid-oceanic ridge that forms the western boundary of the Farallon plate and the Farallon–North America trench moved towards each other and eventually met. Only small segments of the Farallon plate remain at the surface today (Fig. 1). The largest of these remnants are the Juan de Fuca, Cocos and Nazca plates. Most of the North American west coast is now bordered by the Pacific plate. With the arrival of part of the ridge at the trench as of 30 Ma, subduction started to be replaced by Pacific–North America transform motion. This led to the formation of a window in the subducted slab [5]. The final stages of subduction were accompanied by a decreasing age of the subducting Farallon plate and decreasing subduction velocities [6,7]. It is unclear whether this part of the subducted Farallon lithosphere would still have a thermal signature in the mantle today.

Severinghaus and Atwater [8] inferred the thermal state of the subducted Farallon plate by two-dimensional mapping of a thermal parameter, which is a function of the time since subduction and age upon subduction, using the analytical thermal model of McKenzie [9]. They concluded that away from the still actively subducting portions, the Farallon plate should be thermally equilibrated with the surrounding North American upper mantle. However, positive seismic velocity anomalies in the transition zone (Figs. 2 and 3) below North America suggest that there are subducted fragments of the Farallon plate in the upper mantle that are still a few hundred degrees colder than the surrounding mantle [2].

The high velocities imaged in the transition zone below the western USA form a more or less continuous feature with high velocities imaged in the lower mantle [1] (Grand, personal communication, 2001) below the central and eastern US (Fig. 3). The lower mantle anomalies have been associated with the subducted Farallon plate. Dynamic models of mantle convection with imposed plate velocities at the surface give thermal anomalies that correlate well with seismic anomalies seen in the lower mantle [3,10]. These global studies do not address the smaller scale anomalies imaged in the transition zone.

Our objective is to model the present thermal signature of the Farallon plate in the upper mantle. We investigate to what extent the subducted plate is thermally equilibrated with the surrounding mantle and how much of it could be detectable by seismic tomography. To obtain the thermal structure we use a kinematic model in three-dimension, based on the history of plate motions and reconstructed plate ages. The resulting thermal structure is converted to seismic velocity structure. The tomographic resolvability of the synthetic velocity structure is then tested and the thermal velocity model is compared with the tomographic model NA00 [11,12]. A similar approach has been previously applied to the Mediterranean region and Indonesia [13,14]. The quantitative comparison of the tomography and the thermal model allows us to determine which

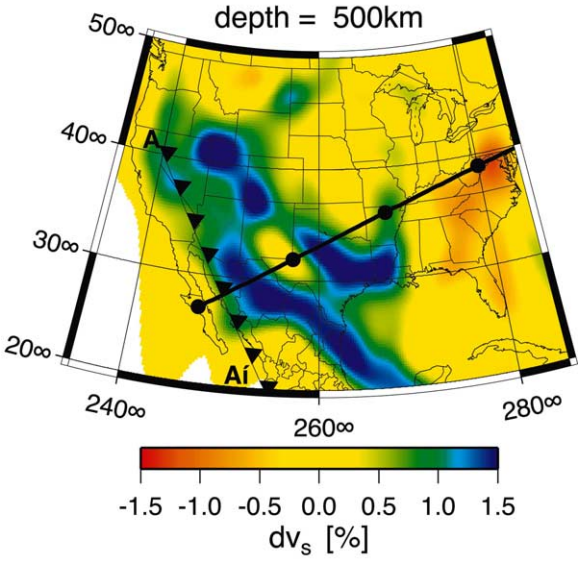

Fig. 2. Horizontal section at 500 km depth through NA00 [12]. Line with triangles marks the trench location used in the kinematic model. The line with dots (at 10° intervals) shows the location of the cross section in Fig. 3.

part of the Farallon plate is actually imaged in the upper mantle below North America. Constraints on the location and amount of subducted material in the upper mantle help to understand the dynamics of the slab in the transition zone.

2. Model constraints

As input for the kinematic thermal model we need plate velocities, plate ages at the trench and the subduction geometry. Constraints on the first two come from plate tectonic reconstructions for the past 60 Myr, which is sufficient to analyze the upper mantle part of the subducted Farallon plate. The geometry of subduction will be discussed in Section 3.

2.1. Plate kinematics

We calculate the Euler poles of the Farallon plate relative to a fixed North America by combining the poles for the Pacific–Farallon spreading [15] with the Pacific–North America global plate circuit poles of Norton [16]. The poles of Royer et al. [15] were used because of their consistency with the age grid of Müller et al. [17] used for deriving plate ages. We assume that spreading occurred symmetrically. By using one single spreading pole for every point in time, we ignore the fact that the Farallon plate broke up after the ridge met the trench. This is justified since the movements of the plate fragments were similar until ~15 Ma [18]. Furthermore, due to the slab window formation, there are only poles available for the northern and the southern parts but not for the central part of the subduction and the simplest kinematic scenario is the assumption of a single coherent plate.

In order to calculate the Farallon velocities relative to North America, it is necessary to first define the trench location. This location is not coincident with the present west coast of North America, due to around 300 km of Basin and Range extension in the middle and late Cenozoic [19]. Severinghaus and Atwater [8] reconstruct the position of the trench for several points in time. We use their location at 30 Ma, shown in Fig. 2, which is a reasonable average position for the past 60 Myr. The southern end of this trench ex-

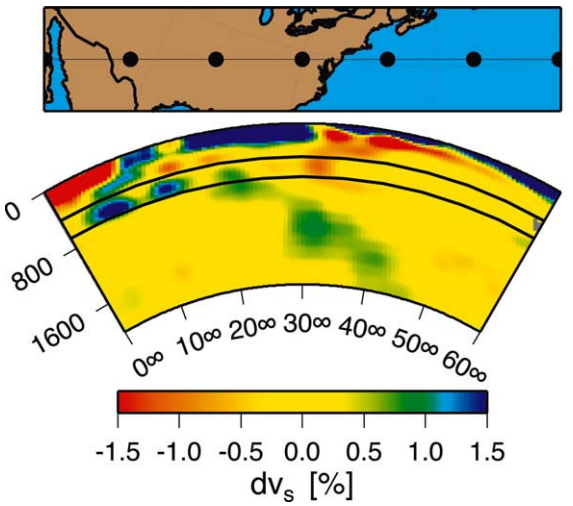

Fig. 3. Combined cross section through the tomographic S-velocity models NA00 [11,12] (above 660 km) and the model of Grand [1] (Grand, personal communication, 2001; below 660 km). Bold lines mark the 660 km and the 400 km discontinuity. Velocity anomalies are relative to PEM-C [46] in the upper mantle, to PREM [36] in the lower mantle. The color scale is saturated for stronger anomalies than + or −1.5% as occur in the uppermost mantle.

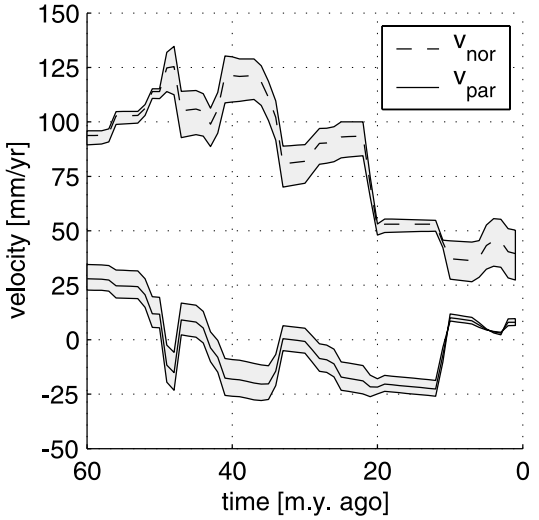

Fig. 4. Perpendicular and parallel components of mean velocity of the Farallon plate relative to North America at the trench (location in Fig. 2) for the past 60 Myr based on poles from [16,15]. The gray area shows the variability of velocity along the trench.

tends to the North America–Cocos (Rivera)–Pacific triple junction, while the northern end lies near the North America–Juan de Fuca–Pacific triple junction (Fig. 2).

The calculated Farallon–North America convergence velocities are shown in Fig. 4, separated into its perpendicular and parallel components relative to the trench. The variability of the velocity along the trench is ±10%, allowing us to use the average value along the trench in the model. The parallel part of the velocity is always significantly smaller than the perpendicular part. The mean value of the parallel component is around 20% of the velocity. The total displacement due to the parallel component does not exceed 300 km. We will neglect trench parallel movement in the thermal modeling, as the motion does not influence thermal structure and has only a small effect on the location of the thermal anomalies relative to North America. From 60 to 20 Ma, the convergence velocity is often higher than 10 cm/yr, which is at the higher end of present-day convergence rates for subduction zones around the world [20]. After 20 Ma, convergence slows down to the values of 3–4 cm/yr currently observed for the Juan de Fuca plate.

To estimate the uncertainties, we compared our velocities with velocities obtained by using other published poles [6,7]. The poles in Stock and Molnar [7] are also derived from the global plate circuit, those in Engebretson et al. [6] are based on the fixed hotspot reference frame. Over the past 60 Myr, the velocities we use are on average 0.1 cm/yr larger than those of Stock and Molnar [7] and 0.3 cm/yr smaller than those of Engebretson et al. [6]. Thus the total estimated length of slab does not change much when a different set of poles is used. At any one point in time the differences between the velocities estimated with the different plate motion models may be larger. The most striking difference is between 40 and 60 Ma, where our already high convergence velocities are ~4.0 cm/yr lower than the values from Engebretson et al. [6].

The length of subducted plate produced by the history of plate motions is shown in Fig. 5. The high convergence velocities produced 5000 km of subducted Farallon plate over the past 60 Myr. Almost 2000 km of Farallon plate were subducted after the ridge first met the trench around 30 Ma.

2.2. Plate ages

To obtain the age of the Farallon plate at the trench we created a synthetic Farallon plate by

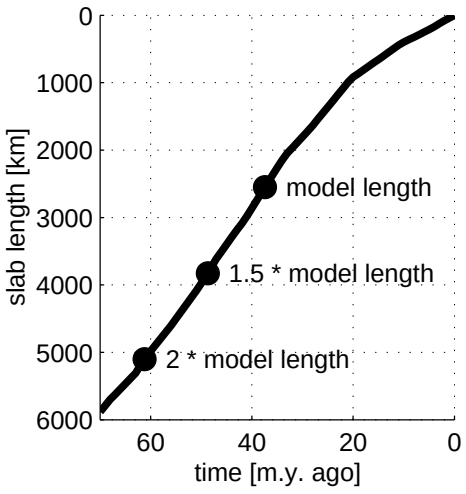

Fig. 5. Slab length as a function of time following from the average convergence velocity shown in Fig. 4.

rotating the Pacific isochrons [17] with finite rotation poles of the Pacific–Farallon spreading [15]. We then rotate the synthetic plate back to its past position relative to North America and read out the age values along the trench.

Fig. 6 shows the age of the Farallon plate at the trench for the past 60 Myr. The variability of the lithospheric age along the trench is much higher than that of the velocities (Fig. 4) and is the cause for significant lateral variations in thermal structure of the slab. The slab window that starts to evolve shortly after 30 Ma is clearly visible. The uncertainties in the ages depend on the uncertainties in the velocities and therefore we also compared age maps obtained with a different set of poles [7]. Differences were within ± 10 Myr, except near transform faults, where the differences can be higher due to differences in transform location.

3. Kinematic thermal modeling

3.1. Temperatures

To determine the consequences of the known plate motions for subduction-related thermal

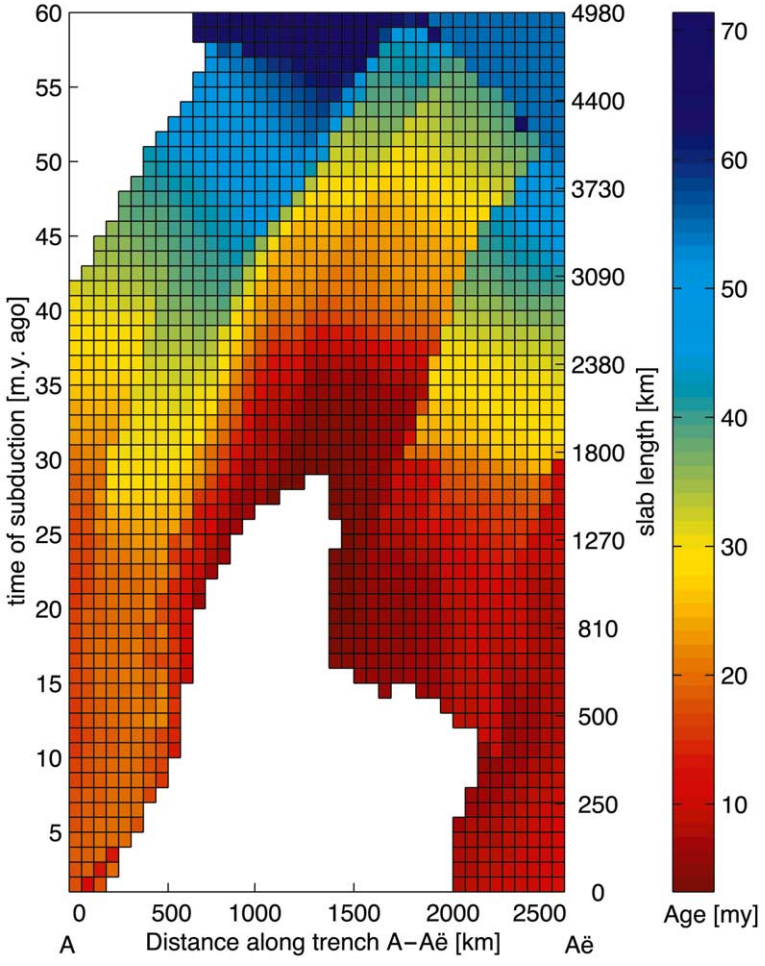

Fig. 6. Age of the Farallon plate consumed at the trench during the past 60 Myr. Colors show the age of the lithosphere that was consumed at a particular point in time and position along trench (location in Fig. 2). For the white area in the upper left no data are available. In the model an average value from neighboring points was used for this region. The white area in the bottom center corresponds to the slab window. The notable age discontinuities are due to transform faults.

anomalies in the mantle we solve the three-dimensional energy equation:

$$\frac{\partial T}{\partial t} = \vec{\nabla}\cdot\kappa\vec{\nabla}T - \vec{v}\cdot\vec{\nabla}T + \frac{A}{\rho_M C_p} + \frac{\alpha g T v_z}{C_p} \qquad (1)$$

Here T is temperature, t time, κ thermal diffusity, v velocity, A heat production, ρ_M mantle density, C_p specific heat, α thermal expansivity, g gravitational acceleration and v_z the vertical velocity component. Adiabatic heating ($\alpha g T v_z/C_p$) is included to obtain real rather than potential temperatures. We neglect viscous heating, which has been shown to be small for the constant viscosity flow field that we use [21]. The effects of phase transitions are also neglected, since latent heat in a pyrolite composition induces temperature jumps no more than 50 K [22]. Variable thermal conductivity [23] was also tested, but the effect was small for the plate dips and velocities we used.

Eq. 1 is solved numerically on a Cartesian grid in three-dimension. Following Trompert and Hansen [24], we use a finite volume discretization in space, together with a Crank–Nicholson scheme and second-order upwind in time and a multigrid solver with damped Jacobi as a smoother. The model was compared with published thermo-kinematic models [21,23,25–27].

The calculations start with an adiabatic mantle with a potential temperature of 1300°C, to which we add a subducting plate with the thermal structure of 60 Myr old oceanic lithosphere and a continental overriding plate. Temperatures in the oceanic lithosphere as a function of age are calculated using the boundary layer model with a constant basal heat flux [28].

The origin of our box is located at the surface at point A′ shown in Fig. 2. We used a grid dimension of $512\times64\times128$ points corresponding to 5440 km in x-direction (perpendicular to the trench) by 2560 km in y-direction (along the trench) by 1000 km in z-direction (vertical). Grid spacing ranges from 5.5 to 12 km in x-direction and 5 to 7 km in z-direction. In y-direction it is possible to use a constant large spacing of 40 km since there are only conductive fluxes in this direction (trench parallel motion being neglected).

At the top boundary ($z=0$) temperature is kept at 0°C, except at the ridge where temperature is set to the potential mantle temperature $T=T_m=$ 1300°C. At the bottom a temperature gradient of $0.5\cdot10^{-3}$°C m^{-1} is imposed, consistent with an adiabatic temperature gradient. We assume $\partial T/\partial y = 0$°C/m at the box boundaries $y=0$ and $y=$ 2560 km. At the boundary at $x=5040$ km temperature is fixed to a continental geotherm with a surface heat flow of 60 m Wm^2 [29] for the 90 km thick lithosphere and a 1300°C adiabat for the mantle. On the boundary at $x=-400$ km we prescribe temperatures of the incoming oceanic lithosphere consistent with the evolution of plate age along the trench through time (Fig. 6) and a 1300°C adiabat. In the overriding plate, heat production consistent with the continental geotherm is included [29]. In Table 1, the values of the geothermal parameters that were used are listed.

The subduction geometry through time, i.e. the path of the slab through the mantle, is controlled by slab–mantle dynamics, which are not well understood. Geological data and seismic tomography provide some constraints on the evolution of slab geometry. For example, the leading edge of the slab window is residing in the upper mantle [2]. The horizontal extent of the slab window for a 0° slab dip is shown in Fig. 1. Any model slab dips steeper than about 20° would put the leading edge of the slab window into the lower mantle. For the thermal modeling we chose to use a constant dip of 15°, which connects the trench location with the present-day entry point of the slab into the lower mantle as fixed by Grand's model [1] (Grand, personal communication, 2001) (Fig. 3). The thermal anomalies of the subducted material are controlled by the time since subduction and by the age upon subduction and not by the

Table 1
Thermal modeling parameters

Name	Value	Unit
Thermal diffusity (κ)	10^{-6}	m^{2}s^{-1}
Mantle density (ρ_M)	3300	kg m^{-3}
Specific heat (c_p)	1050	J kg^{-1}°C^{-1}
Thermal expansion coefficient (α)	$3.3\cdot10^{-5}$	°C^{-1}
Potential mantle temperature	1300	°C
Basal adiabatic heatflux	$2.5\cdot10^{-2}$	W m^{-2}
Mantle heatflux at base of plate	$9.3\cdot10^{-3}$	W m^{-2}
Heat production (A)	$2.0\cdot10^{-6}$	W m^{-3}

exact trajectory followed by the subducted material. Thus, even though our model geometry may not correspond to the geometrical slab evolution, the anomalies as a function of time since subduction are constrained by our modeling. The possible evolution of the slab geometry is discussed in Section 5, based on geological constraints and discrepancies between the geometry of the thermal model and the tomography. For a rigid continuous slab with a constant 15° dip, the material now at a depth of 660 km in the model subducted at 37 Ma. The model is started 60 Ma in order to avoid any influences on the present-day thermal structure from the initial model.

3.2. Velocity field

The velocity field is input and must satisfy the continuity equation

$$\vec{\nabla}\cdot\vec{v} = 0. \quad (2)$$

Due to the use of the finite volume technique, satisfying Eq. 2 for each grid cell is important to avoid instabilities in the solution.

The input velocity field is illustrated in Fig. 7, superimposed on the temperature solution for a cross section at $y \sim 1250$ km, approximately through the center of the slab window (Fig. 6). The overriding continental lithosphere is kept fixed down to 90 km depth. The subducting plate is entered from the left side of the model ($x = -400$ km) according to the trench-perpendicular velocities from Fig. 4. Variations in average velocity through time are incorporated, and result in the decrease of velocities with time seen in Fig. 7. For the mantle above and below the slab we use a two-dimensional analytical solution for corner flow in a constant viscosity mantle ([30], p. 250–251). This velocity field, corresponding to active subduction, is shown in the panels for 40 and 30 Ma (Fig. 7). After subduction of the youngest edge of the plate we assume no more surface plate convergence in the slab window and no flow in the mantle at depths less than the top of the sinking slab. The rest of the slab moves with the same velocity as the still actively subducting part of the plate, so that the integrity of the slab along strike is maintained. Mantle flow is again calculated analytically. This velocity field for the sinking part of the slab is shown in the cross sections for 20 Ma, 10 Ma and the present day.

The assumption of no flow above the sinking slab provides a first-order model for the thermal structure within the slab window. If mantle flow were dragged into the window by the sinking slab, cool isotherms would be drawn down behind the sinking slab leading to cooler temperatures in the slab window than the model shown. If mantle flow filled the slab window with warmer material, temperatures within the window might be warmer than modeled now. Flow in the mantle wedge above the slab may be more complex than the constant viscosity solution used here. This can have significant effects on the thermal structure of the mantle wedge (e.g. [31]), but is expected to have only a minor influence on the temperatures of the slab itself.

4. Thermal modeling results

4.1. Thermal structure of the Farallon slab

The evolution of the thermal structure through time (Fig. 7) shows that the thermal anomaly associated with subduction decreased significantly as the subducted material became younger in age and active subduction ceased. At 40 Ma, upper mantle slab anomalies exceed 600°C, while at 0 Ma the anomalies are only 200–300°C. Furthermore, while initially the thermal anomaly decreased with depth, at the final stages the effects of the slab window and decreasing lithospheric age dominate and anomalies are smallest above 400 km and increase in the transition zone.

Fig. 8a shows the present-day thermal structure, in a dip-parallel slice, roughly through the core of the low-temperature anomaly. Only upper mantle thermal anomalies below 100 km (i.e. below the continental lithosphere) are shown. All of the subducted plate still has a thermal anomaly in the range of 200–400°C. Thus the subducted material is not thermally equilibrated and these thermal anomalies are still sufficient to introduce a significant viscosity and seismic velocity contrast

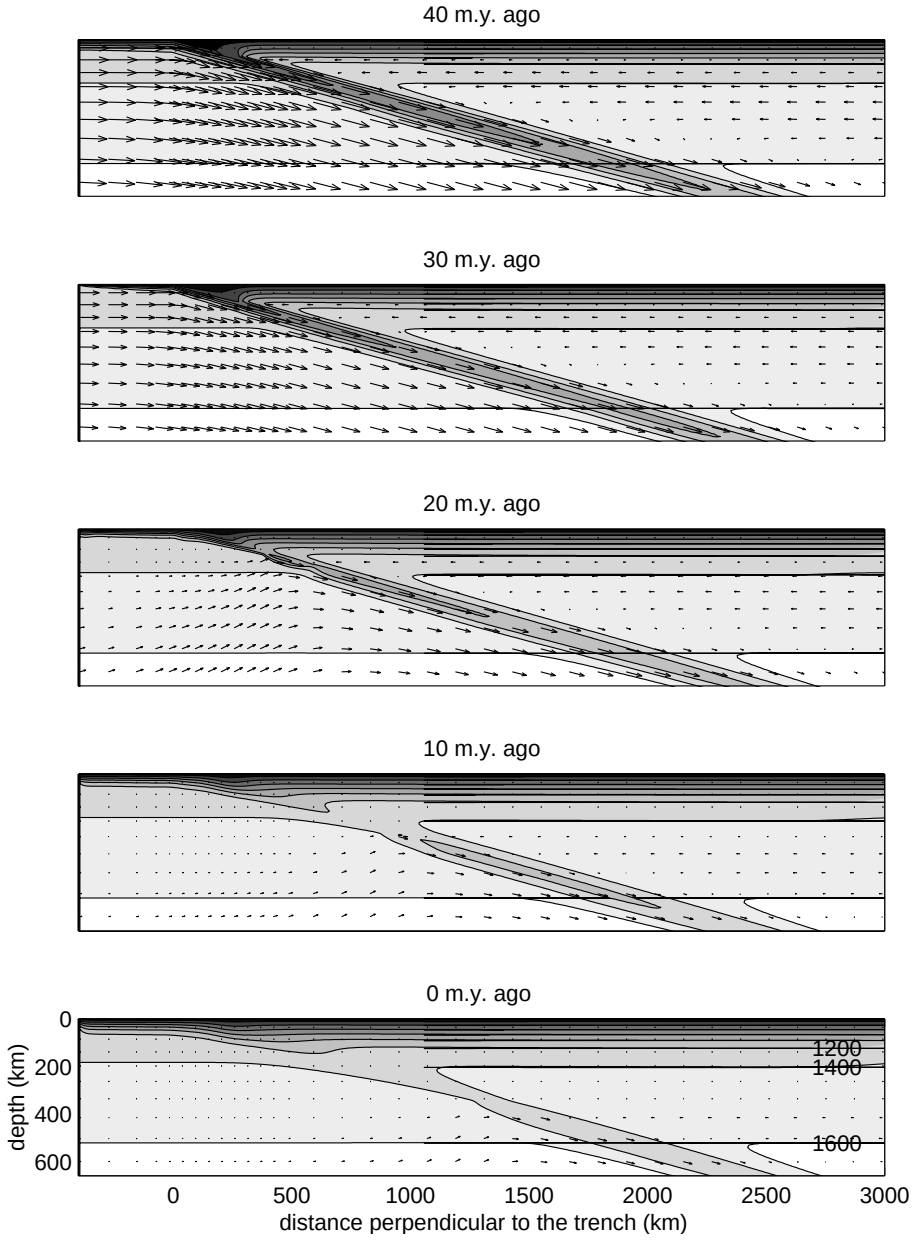

Fig. 7. Two-dimensional cross sections at different times of the model run, perpendicular to the trench at position $y = 1250$ km from point A′ (Figs. 2 and 6), close to the middle of the slab window. The trench is located at $x = 0$ km. Only the upper mantle part of the model is shown. The cross section at 0 Ma corresponds to the present day. Black arrows illustrate the velocity field every tenth grid point and are scaled according to velocity size, with the largest arrow corresponding to the maximum velocities 40 Ma, i.e. 12 cm/yr (Fig. 4). Temperature contours are drawn every 200°C.

with the surrounding mantle. The actively subducting parts of the slab have larger thermal anomalies of 500–600°C, but only down to about 200 km depth. Within the slab window, temperatures are 100 to 200°C cooler than the surrounding mantle. These temperatures may be somewhat underestimated or overestimated due to the assumed absence of flow into the slab window.

The analytical model used by Severinghaus and Atwater [8] keeps the temperatures at the slab boundaries fixed thus not allowing the slab to cool off the surrounding mantle. Slab temperatures from this model therefore represent an upper estimate. Nevertheless the results from Severinghaus and Atwater [8] are not inconsistent with our thermal slab structure. They defined assimilation of the slab based on the cessation of seismicity, assuming that the presence of seismicity is related to a significant temperature-controlled rheological difference between the slab and the surrounding mantle. The seismicity cut-off corresponds to a thermal anomaly of about 600°C [32]. Indeed most of the subducted lithosphere is warmer than this. But the thermal anomalies are large enough for this lithosphere to be coherent and to be detectable by seismic tomography.

4.2. Synthetic seismic velocity structure

To compare the thermal anomalies of our model with the S-wave velocity anomalies from tomography, we convert the modeled temperatures to S-wave velocities. We use an update [33] of the

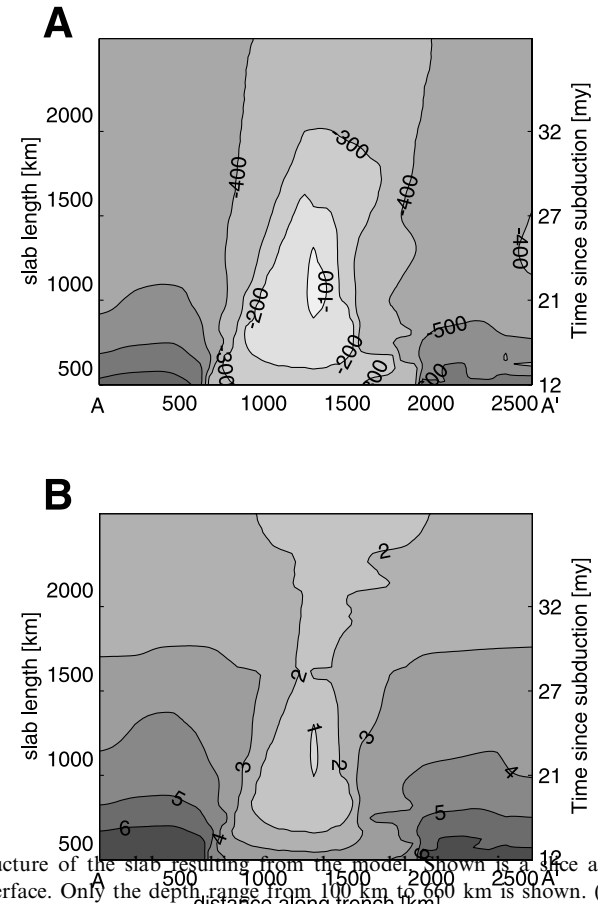

Fig. 8. Present-day thermal structure of the slab resulting from the model. Shown is a slice along the top of the slab, looking down-dip at the slab-mantle interface. Only the depth range from 100 km to 660 km is shown. (a) Temperature difference relative to the right side of the model. (b) Resulting shear wave velocity anomaly in %.

method and data used by Vacher et al. [22]. The conversion assumes a pyrolitic composition for the whole upper mantle. A harzburgitic lithosphere is slightly faster than pyrolite; on the other hand, oceanic crust has lower velocities than pyrolite in the transition zone [33]. Overall, the effect of composition is secondary to the effect of temperature [33,34]. The phase transitions in olivine and garnet/pyroxene components are fixed to take place at 400, 520 and 660 km depth. The effect of anelasticity was included following Karato [35], with a frequency dependence $a = 0.15$, quality scaling factor $Q_0 = 0.5$ and parametrization of the activation energy in terms of melting temperature with a scaling factor $g = 30$. This results in an anelasticity profile similar to the $Q_S(z)$ of PREM [36] for a 1300°C mantle adiabat. A different set of anelasticity parameters does not significantly affect our conclusions as long as the profile for the mantle adiabat is close to the Q_S of PREM and other one-dimensional Earth models. S-wave velocity anomalies are calculated relative to the velocities along a 1300°C mantle adiabat. This choice of a reference model is motivated by the agreement between synthetic seismic velocities for a ~1300°C mantle adiabat and one-dimensional seismic reference models [37]. Furthermore, positive velocity anomalies dominate in tomographic models of the North American transition zone, consistent with a subduction-related origin.

Fig. 8b shows the resulting S-velocity anomalies for the same slice as shown in Fig. 8a. All of the thermal anomalies related to the subducted Farallon plate result in significant V_S anomalies of ~2% or more. The velocity signature is not simply the thermal signature multiplied by a constant scaling factor. Due to a decreasing sensitivity of velocity to temperature with depth, velocity anomalies decrease with depth more strongly than the thermal anomaly in the actively subducting parts of the plate and velocity anomalies hardly increase with depth below the slab window.

5. Comparison with seismic tomography

We compare the amplitude and the location of the velocity anomalies obtained from the thermal kinematic model with the tomographic anomalies in the upper mantle as imaged in model NA00 [12,34]. Since the geometry of the tomographic anomalies (Figs. 2 and 3) and the thermal model (Figs. 7 and 8) are different, a slice by slice comparison is not possible. However, a comparison of the total volume of the positive, i.e. subduction-related, velocity anomaly imaged in the upper mantle allows us to constrain which part of the subducted Farallon plate is actually imaged by the upper mantle tomography. This result, together with a comparison of the anomaly locations, provides constraints on the evolution of slab geometry in the transition zone.

5.1. Amplitude of the anomalies

To obtain constraints on the total amount of subducted material present in the upper mantle, positive seismic velocity anomalies are integrated over the length and width of the thermal model, and the corresponding region between 25°N and 50°N in NA00. All mantle heterogeneity not associated with the subducted Farallon plate, e.g. structure due to the North American lithosphere, is excluded by limiting the depth range of integration to below 350 km for NA00, and below 225 km in the thermal model. The depth ranges reflect the difference in slab geometry in the tomographic and the thermal model.

To assess how much of the difference between model and tomographic anomalies is due to limited resolving power in the tomographic imaging, we performed a resolution test. For this test the modeled velocity anomalies were projected onto geographical coordinates and synthetic seismic data were computed using the same data coverage as used to derive model NA00. These synthetic data were then subjected to the same tomographic inversion procedure as NA00. The resolution test shows that, despite the effects of damping and smoothing, the temperature anomalies of the kinematic model are detectable by the seismic data used to derive NA00.

The ratio of the integrated velocity anomaly from NA00 and the anomaly derived from the thermal model is 1.2 (Fig. 9a). The volume integral of the resolved subduction-related positive

velocity anomalies is 1.6 times lower than in the input from the thermal model. If this is taken as a measure for the limited resolution the integrated anomaly in NA00 exceeds the model anomaly by a factor 1.9.

Peak anomalies in the velocities derived from the thermal model are about 1.5 times higher than in NA00, but NA00 has a larger amount of low amplitude anomalies (Fig. 9b). Furthermore, in NA00 a steady linear decrease from a large number of low amplitude anomalies to a small number of strong anomalies is observed. In the thermal model this decrease is not linear; the number of points with anomalies in the range from 50 ms^{-1} to 100 ms^{-1} is constant. Due to damping and smoothing applied in the tomographic inversion, peak anomalies in the resolved output model are 2.6 times lower than in the input from the thermal model. The distribution of the amplitudes of the velocity anomalies after the resolution test, a steady decrease, resembles NA00 more than the input model.

The amplitude of the integrated thermal anomaly depends predominantly on the length of subducted Farallon slab in the upper mantle, and is hardly influenced by the position of the slab material within the mantle. The conversion to seismic velocities, however, varies with depth, which makes the amplitude of the integrated synthetic velocity anomaly dependent on the depth at which the subducted material is located. The thermal model anomaly is present throughout the depth of the upper mantle, while the imaged anomalies in NA00 that are interpreted as slab remnants are concentrated in the transition zone (Fig. 9a). Thus the total velocity anomaly estimated from our thermal model is likely an overestimate, since bringing the thermal anomalies to larger depths would decrease the associated velocity anomalies. Taking this into account, the integrated anomaly in NA00 exceeds the model anomaly by an even larger amount. If we restrict the depth range to be 350 to 650 km in the thermal model and the output model of the resolution test, we obtain a ratio of about 2.5 between NA00 and the resolved model anomalies.

The resolution correction of 1.6 is only an estimate. The damping and smoothing done in tomographic inversions generally leads to an underestimate of total anomaly amplitudes. But, for example, ignoring the influence of mode coupling may lead to an overestimate of high velocities below a low velocity region such as the western US [38]. Also, a flat lying slab (as seen in NA00)

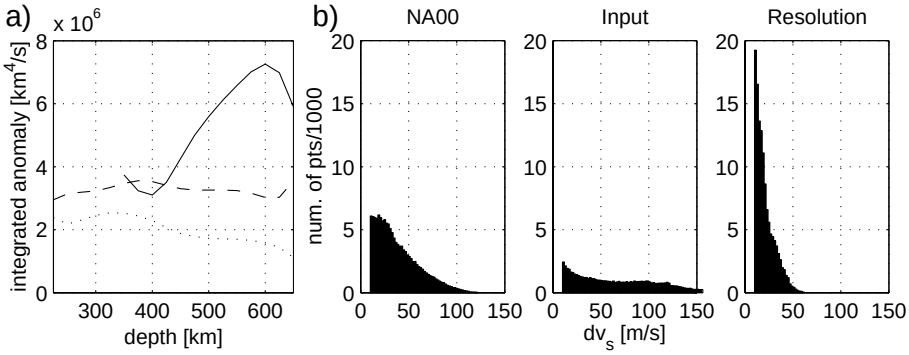

Fig. 9. Comparison of integrated positive anomalies in the tomographic model NA00 with the velocities derived from the thermal model before and after a tomographic resolution test. Depth range is 350–650 km for NA00, 225–650 km for the thermal model and the resolution test. Only points located between 25°N to 50°N were considered in NA00, in all three cases only anomalies bigger than 10 m/s where considered. All data points are on the same grid, so that it was possible to simply sum up the anomalies. (a) Integrated velocity anomalies per 25 km thick depth layer as a function of depth. Integrated anomaly (km^4/s) over the whole depth range is $6.83 \cdot 10^7$ for NA00, $5.89 \cdot 10^7$ for the thermal model and $3.58 \cdot 10^7$ for the resolution test. We recover only about half of the integrated input anomaly in the tomographic inversion. (b) Histogram showing the distribution of positive anomalies as a function of amplitude (m/s). Note the shift from a small number of strong anomalies to a large number of small anomalies between input and resolution.

is better resolvable than a dipping slab. Resolution further varies laterally and the location of the anomalies in NA00 is not exactly the same as in the thermal model used as input for the resolution test. Given all these uncertainties, the thermal model predicts an upper mantle seismic velocity anomaly that is about 1.5 to 2.0 times smaller than what is imaged by seismic tomography.

In order to produce the larger anomaly imaged in NA00 more cold material is needed in the upper mantle, material that subducted earlier than 37 Myr ago. Assuming that imaged slab volume scales with slab length, we can estimate from Fig. 5 a time since subduction between 50 and 60 Myr for the oldest parts of the slab still residing in the upper mantle. A maximum length, not thickened, continuous slab that connects the trench and the top of the seismic anomaly in the lower mantle would correspond to 43 Myr of subducted material, only slightly more than in the thermal model. Thus the amount of slab material in the upper mantle implied by the observed seismic anomalies (50 to 60 Myr of slab) requires significant internal deformation of the slab in the transition zone.

5.2. Location of the anomalies

Although we did not attempt to model slab geometry, a comparison of our geometrically first-order model with the location of tomographic velocity anomalies provides some insight. In our model the slab window reaches to a depth of about 400 km (Fig. 7). This is roughly consistent with the tomographic images of Van der Lee and Nolet [2,11], which show mainly low velocities under the western United States down to 350 km, indicating the absence of slab above this depth. Although the depths of the modeled slab material are reasonable, most of the slab-related anomaly in the tomographic model is located west of that in our thermal model. This indicates that we use a horizontal subduction component relative to North America that is too large on average. The horizontal velocities in our thermal model are determined by the subduction velocities, which follow from the plate motions assuming a rigid, coherent plate. Since we find that all of the slab should be seismically detectable, the westernmost edge of the imaged high velocity material must coincide with the leading edge of the slab window. Horizontal velocities of this westernmost imaged material relative to North America must have been about one-quarter of the convergence velocity of the subducting parts of the Farallon plate north and south of the slab window. This difference in subduction velocity indicates that the slab was not moving as a rigid, coherent body.

The thermal structure of the subducted Farallon plate is controlled by the relative convergence between the Farallon and North American plates. However, the absolute movement of North America relative to a hotspot reference frame influenced the geometry of the subducting Farallon plate through time and thereby the location of the seismic anomalies. According to the poles given in Müller et al. [39], North America's absolute movement in the Cenozoic was about 2.5 to 3 cm/yr in a southwest direction and roughly opposite to the Farallon absolute movement. The total displacement of North America relative to the hotspots amounts to approximately 1700 km for the past 60 Myr. However, only if accompanied by internal plate deformation do the absolute motions lead to a different relative velocity between the subducted Farallon and North America than between the surface Farallon plate and North America.

5.3. Evolution of slab geometry

Fifty to sixty Ma was a special time in the geologic history of North America. From the mid-Jurassic until ~80 Ma volcanism and mountain building processes were concentrated along the coast, indicating a normal slab dip [18]. After 80 Ma, the volcanic belt shifted to the east by about 1000 km over the period of several million years [18]. The hypothesis of a flattening subducting slab is the most likely explanation for the eastward shift of magmatism [18]. This eastward shift coincides in time with the far inland occurring Laramide orogeny (70–50 Ma) [40]. It is reasonable to assume that the flat subduction and the Laramide orogeny are linked [41]. The magmatic record indicates that the episode of flat slab sub-

duction ceased after ~20 to 30 Myr, when around 40 Ma (depending on the latitude) the volcanic belt shifts back to the west [18]. This westward shift of magmatism is less sharply defined in time than the preceding eastward shift. Basin and Range extension in the middle and late Cenozoic has been linked to the removal of the flat slab and the subsequent influx of warm mantle [18].

Several causes for slab flattening during the Laramide orogeny, have been proposed: (1) an increase in the westward component of North America's absolute plate velocities [6,39] leading to trench roll-back and lithospheric doubling [42], (2) increased buoyancy of the slab, for example, through the subduction of an oceanic plateau with an anomalously thick crust [18]. Convection modeling [43] demonstrates that flat subduction on the scale inferred for North America at 70–50 Ma probably requires a combination of (1) and (2).

The same mechanisms may also affect the transition of the slab through the endothermic phase transition and viscosity increase at 660 km depth. According to Christensen [44] an oceanward trench migration velocity of 2.5–3 cm/yr is just high enough to inhibit penetration into the lower mantle. The stalling of slab penetration in his models is the result of slab flattening at the base of the transition zone. A flat slab geometry inherited from the phase of flat subduction would have a similar effect. Slab buoyancy due to an anomalously thick oceanic crust may also affect the transition into the lower mantle. The phase transition to perovskite+magnesiowüstite in oceanic crust occurs at a depth larger than in the surrounding mantle. Therefore, oceanic crust, which throughout most of the upper mantle is denser than the rest of the lithosphere, is relatively buoyant around 660 km depth [45]. If the oceanic crust is sufficiently thick, the crustal buoyancy may become a factor that hinders penetration into the lower mantle. We infer that penetration of the slab into the lower mantle stalled around 60 Ma, which is later than the start of trench roll-back around 80 Ma. [16,18]. The roll-back by itself was seemingly not sufficient to stop the transfer of slab material into the lower mantle. The extra buoyancy and geometry of the flat slab may have been the factors that ultimately impeded further penetration. The cartoon in Fig. 10 summarizes the possible evolution of the subducted Farallon plate. Significant internal deformation is necessary to accommodate the large amount of slab material that subducted after penetration into the lower mantle was impeded. Continued trench roll-back resulted in the accumulation of most of this material at the base of the transition zone.

Internal deformation of the Farallon slab in the transition zone would be facilitated by the relatively high slab temperatures (Figs. 7 and 8a). The non-uniform transition zone anomalies (Figs. 2 and 3) may be an expression of slab buckling and/or fragmentation. Such deformation may produce additional heat and fragmentation leads to the formation of smaller segments that will be

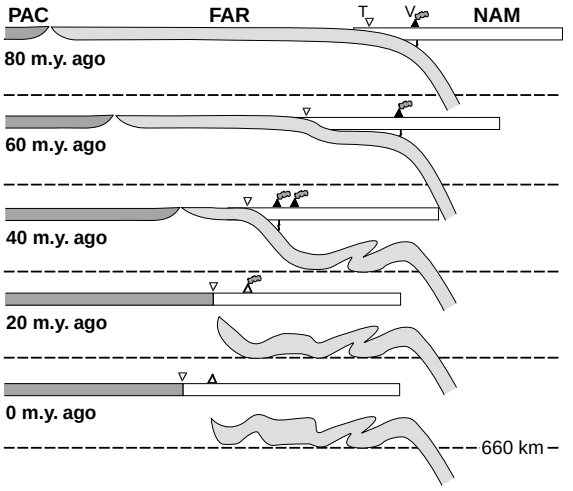

Fig. 10. Cartoon of Farallon slab evolution in the upper mantle in a fixed hotspot reference frame. Abbreviations: T, trench; V, volcanoes. Only a small part of the lower mantle slab is shown. Consumption of the Farallon plate is the result of absolute motion of both the Pacific–Farallon ridge and the North American plate. After 80 Ma flat subduction is initiated and volcanism shifts far land inward. Around 40 Ma the slab steepens again and volcanism migrates back towards the trench. The flatly subducted part of the slab apparently resisted penetration through the 660 km discontinuity and caused internal slab deformation in the transition zone. In reality this deformation was a complex three-dimensional process.

warmed up faster and therefore the resulting anomaly would be smaller than modeled, requiring even more slab material to be accumulated in the transition zone. On the other hand, slab thickening could slow the rate of conductive cooling compared with cooling of an undeformed slab.

6. Conclusions

Lower mantle seismic velocity anomalies due to subduction of the Farallon plate [1] (Grand, personal communication, 2001) have been quantitatively predicted from the long history of subduction [3,10]. The thermal anomaly of the upper mantle Farallon slab, however, has qualitatively been predicted to be small based on the young age, high subduction velocities and the formation of the slab window after the Farallon–Pacific ridge collided with the Farallon–North America trench [8]. Nevertheless, high velocities have been imaged in the transition zone beneath North America and interpreted as representing the subducted trailing fragments of the Farallon plate [2]. We have modeled the thermal signature of the subducted Farallon plate in the upper mantle based on the Cenozoic plate tectonic history to investigate to what extent the slab is thermally equilibrated and which part of the subducted plate could correspond to the mapped seismic anomalies.

The following conclusions can be drawn:

1. All of the subducted Farallon plate in the upper mantle has a thermal anomaly of 200–400°C. Thus, the plate is not thermally equilibrated with the surrounding mantle, although the thermal anomalies are smaller than those for an actively subducting plate. The thermal signature is sufficient to produce a detectable seismic velocity anomaly, and a significant rheological contrast with the mantle.
2. The proximity of some of the tomographic anomalies to the trench requires that part of the plate at depth did not move with the same convergence velocity as the plate fragments at the surface. The subduction velocity of the slab at depth thus varied significantly along strike for at least part of the past 60 Myr, possibly in response to the development of the slab window after ridge–trench collision started.
3. Analysis of the volumetrically integrated seismic velocity anomaly shows that 1.5 to 2.0 times more material is imaged in the upper mantle seismic tomography than predicted by the thermal model for a continuous undeformed slab. In the kinematic thermal model the oldest material in the upper mantle subducted $\sim$40 Myr ago. Assuming that volume scales with slab length, the tomographic model requires a time since subduction between 50–60 Myr for the oldest parts of the slab residing in the upper mantle. This indicates that the Farallon plate is also internally deformed in the down-dip direction. The deformation of the slab in the transition zone is probably caused by the same mechanisms that were responsible for flat subduction around 60 Ma. Firstly, anomalous slab buoyancy and geometry may impede slab penetration into the lower mantle. Secondly, the trenchward movement of the overriding plate would have led to an accumulation of most of the subducted material at the base of the transition zone, thus providing an additional hindrance to slab penetration.

The comparison of forward modeled thermal structure based on plate motions with seismic velocity images provides a powerful tool to obtain constraints on the evolution of a plate after subduction. Such constraints are important for understanding the role of slabs in mantle dynamics, and for the case of the Farallon plate provide insight in the dynamics of the slab in the transition zone.

Acknowledgements

We thank Steve Grand for making his velocity model available. We thank James Conder, Rob Van der Voo and an anonymous reviewer for their constructive comments.*[SK]*

References

[1] S.P. Grand, Mantle shear structure beneath the Americas

and surrounding oceans, J. Geophys. Res. 99 (1994) 11591–11621.
[2] S. Van der Lee, G. Nolet, Seismic image of the subducted trailing fragments of the Farallon plate, Nature 386 (1997) 266–269.
[3] H.P. Bunge, S.P. Grand, Mesozoic plate motion history below the northeast Pacific Ocean from seismic images of the subducted Farallon slab, Nature 405 (2000) 337–340.
[4] S. Van der Lee, C. Lithgow-Bertelloni, G. Nolet, The subducted trailing fragments of the Farallon Plate, IRIS Workshop Abstract, 1996.
[5] W.R. Dickinson, W.S. Snyder, Geometry of subducted slabs related to San Andreas Transform, J. Geol. 87 (1979) 609–627.
[6] D.C. Engebretson, A. Cox, R.G. Gordon, Relative Motions Between Oceanic and Continental Plates in the Pacific Basin, Geol. Soc. America, Boulder, Colorado, 1985, 59 pp.
[7] J. Stock, P. Molnar, Uncertainties and implications of the late Cretaceous and Tertiary position of North America relative to the Farallon, Kula and Pacific plates, Tectonics 7 (1989) 1339–1384.
[8] J. Severinghaus, T. Atwater, Cenozoic geometry and thermal state of subducting slabs beneath western North America, in: B.P. Wernicke, Ed., Basin and Range Extensional Tectonics near the Latitude of Las Vegas, Nevada, Geol. Soc. Am. Memoir 176, Boulder, Colorado, 1990, pp. 1–22.
[9] D.P. McKenzie, Temperature and potential temperature beneath island arcs, Tectonophysics 10 (1970) 357–366.
[10] C. Lithgow-Bertelloni, M.A. Richards, The dynamics of Cenozoic and Mesozoic plate motions, Rev. Geophys. 38 (1998) 27–78.
[11] S. Van der Lee, G. Nolet, Upper mantle S-velocity structure of North America, J. Geophys. Res. 102 (1997) 22815–22838.
[12] S. VanderLee, High-resolution estimates of lithospheric thickness from Missouri to Massachusetts, USA, Earth Planet, Sci. Lett. 203 (2002) 15–23.
[13] M.R. de Jonge, M.J.R. Wortel, W. Spakman, Regional scale tectonic evolution and the seismic velocity structure of the lithosphere and upper mantle: the Mediterranean region, J. Geophys. Res. 99 (1994) 12091–12108.
[14] E. Hafkenscheid, S.J.H. Buiter, M.J.R. Wortel, W. Spakman, H.M. Bijwaard, Modelling the seismic velocity structure beneath Indonesia: a comparison with tomography, Tectonophysics 333 (2001) 35–46.
[15] J.-Y. Royer, R.D. Müller, L.M. Gahagan, L.A. Lawver, C.L. Mayes, D. Nürnberg, J.G. Sclater, A Global Isochron Chart, 1992.
[16] I.O. Norton, Plate motions in the North Pacific: the 43 Ma. nonevent, Tectonics 14 (1995) 1080–1094.
[17] R.D. Müller, W.R. Roest, J.Y. Royer, L.M. Gahagan, J.G. Sclater, Digital isochrons of the world's ocean floors, J. Geophys. Res. 102 (1997) 3211–3214.
[18] T. Atwater, Plate tectonic history of the northeast Pacific and western North America, in: E.L. Winterer, D.M. Hussong and R.W. Decker, Eds., The Geology of North America, Vol. N, The Eastern Pacific Ocean and Hawaii, Geol. Soc. Am., Boulder, Colorado, 1989, pp. 21–72.
[19] B. Wernicke, G.J. Axen, J.K. Snow, Basin and Range extensional tectonics at the latitude of Las Vegas, Nevada, Geol. Soc. Am. Bull. 100 (1988) 1738–1757.
[20] R.D. Jarrard, Relations among subduction parameters, Rev. Geophys. 24 (1986) 217–284.
[21] J.H. Davies, D.J. Stevenson, Physical model of the source region of subduction zone volcanics, J. Geophys. Res. 97 (1992) 2037–2070.
[22] P. Vacher, A. Mocquet, C. Sotin, Computation of seismic profiles from mineral physics: the importance of non-olivine components for explaining the 660 depth discontinuity, Phys. Earth Planet. Inter. 106 (1998) 275–298.
[23] S.A. Hauck, R.J. Phillips, A.M. Hofmeister, Variable conductivity: effects on the thermal structure of subducting slabs, Geophys. Res. Lett. 26 (1999) 3257–3260.
[24] R.A. Trompert, U. Hansen, The application of a finite volume multigrid method to three-dimensional flow problems in a highly viscous fluid with variable viscosity, Geophys. Astrophys. Fluid Dynamics 83 (1996) 261–291.
[25] M.N. Toksöz, J.W. Minear, B.R. Julian, Temperature fields and geophysical effects of a downgoing slab, J. Geophys. Res. 76 (1971) 1113–1138.
[26] S.C. Ponko, S.M. Peacock, Thermal modeling of the southern Alaska subduction zone: insight into the petrology of the subducting slab and overlying mantle wedge, J. Geophys. Res. 100 (1995) 22117–22128.
[27] A.J. Daniel, N.J. Kusznir, P. Styles, Thermal and dynamic modeling of deep subduction of a spreading center: implications for the fate of the subducted Chile Rise, southern Chile, J. Geophys. Res. 106 (2001) 4293–4304.
[28] M.J.R. Wortel, Age Dependent Subduction of Oceanic Lithosphere, Ph.D. Thesis, Utrecht University, 1980.
[29] D.S. Chapman, Thermal gradients in the continental crust, in: J.B. Dawson, D.A. Carswell, J. Hall and K.H. Wedepohl, Eds., The Nature of the Lower Continental Crust, Geol. Soc. Spec. Publ. 24, Geol. Soc. London, London, UK, 1986, pp. 63–70.
[30] D.L. Turcotte, G. Schubert, Geodynamics: Applications of Continuum Physics to Geological Problems, John Wiley and Sons, New York, 1982, 450 pp.
[31] M.I. Billen, M. Gurnis, A low viscosity wedge in subduction zones, Earth Planet. Sci. Lett. 193 (2001) 227–236.
[32] M.J.R. Wortel, Seismicity and rheology of subducted slabs, Nature 296 (1982) 553–556.
[33] F. Cammarano, S. Goes, P. Vacher, D. Giardini, Inferring temperatures in the upper mantle from seismic velocities, Phys. Earth Planet. Int., submitted.
[34] S. Goes, S. Van der Lee, Thermal structure of the North American uppermost mantle inferred from seismic tomography, J. Geophys. Res. 107 (2002) 10.1029/2 2000JB000049.
[35] S. Karato, Importance of anelasticity in the interpretation of seismic tomography, Geophys. Res. Lett. 20 (1993) 1623–1626.

[36] A.M. Dziewonski, D.L. Anderson, Preliminary reference Earth model, Phys. Earth Planet. Int. 25 (1981) 297–356.
[37] J.J. Ita, L. Stixrude, Petrology, elasticity, and composition of the mantle transition zone, J. Geophys. Res. 97 (1992) 6849–6866.
[38] H. Marquering, R. Snieder, G. Nolet, Waveform inversions and the significance of surface-wave mode coupling, Geophys. J. Int. 124 (1996) 258–278.
[39] R.D. Müller, J.Y. Royer, L.A. Lawyer, Revised plate motions relative to the hotspots from combined Atlantic and Indian Ocean hotspot tracks, Geology 21 (1993) 275–278.
[40] W.P. Lipman, H.J. Protska, R.L. Christiansen, Evolving subduction zones in the Western United States as interpreted from igneous rocks, Science 174 (1971) 821–825.
[41] P. Bird, Formation of the Rocky Mountains, Western United States: a continuum computer model, Nature 239 (1988) 1501–1507.
[42] N.J. Vlaar, Thermal anomalies and magmatism due to lithospheric doubling and shifting, Earth Planet. Sci. Lett. 65 (1983) 322–330.
[43] J. Van Hunen, A.P. van den Berg, N.J. Vlaar, A thermomechanical model of horizontal subduction below an overriding plate, Earth Planet. Sci. Lett. 182 (2000) 157–169.
[44] U.R. Christensen, The influence of trench migration on slab penetration into the lower mantle, Earth Planet. Sci. Lett. 140 (1996) 27–39.
[45] A.E. Ringwood, The role of the transition zone and 660 km discontinuity in mantle dynamics, Phys. Earth Planet. Int. 86 (1994) 5–24.
[46] A.M. Dziewonski, A.L. Hales, E.R. Lapwood, Parametrically simple Earth models consistent with geophysical data, Phys. Earth Planet. Int. 10 (1975) 12–48.